TIME, the Tomographic Ionized-carbon Mapping Experiment: an update on design, characterization, and data from the 2022 commissioning observations

Victoria L. Butler[a], Abigail T. Crites[a,b], Samantha Berek[c], James J. Bock[b,d], Geoff Bower[f], C. Matt Bradford[d,b], Tessalie Caze-Cortes[e], Tzu-Ching Chang[d,b,f], Yun-Ting Cheng[b], Dongwoo T. Chung[c,a], Asantha Cooray[g], Audrey Dunn[e], Nick Emerson[h], Clifford Frez[b], Minal Shaik[a], Francie Wharton[a], Caidan Pilarski[a], Sarah Gates[a], Caleb Greenburg[e], Fiona Hufford[e], Jonathon Hunacek[d], Ryan P. Keenan[h], Baria Khan[c], King Lau[b], Chao-Te Li[f], Ian Lowe[h], Paolo Madonia[b], Dan P. Marrone[h], Evan C. Mayer[h], Lorenzo Moncelsi[b], Sofia Pereira[a], Dang Pham[c], Ibrahim Shehzad[a], Sukhman Singh[a], Guochao Sun[b], Isaac Trumper[h], Anthony Turner[d], Benjamin J. Vaughan[a], Tashun Wei[f], Quinn Wilson[a], Michael Zemcov[e], and (TIME Collaboration)

[a]Cornell University, Ithaca, NY, U.S.A.
[b]California Institute of Technology, Pasadena, CA, U.S.A.
[c]University of Toronto, Toronto, Ontario, Canada
[d]Jet Propulsion Laboratory, Pasadena, CA, U.S.A.
[e]Rochester Institute of Technology, Rochester, NY, U.S.A.
[f]Institute of Astronomy and Astrophysics, Academia Sinica, Taipei, Taiwan
[g]University of California, Irvine, CA, U.S.A.
[h]University of Arizona, Tucson, AZ, U.S.A.

ABSTRACT

We summarize the technical specifications of TIME, the Tomographic Ionized-carbon Mapping Experiment, which is designed to probe the structure and evolution of the universe by using line intensity mapping to measure carbon monoxide (CO) and ionized carbon ([C II]) with a mm-wavelength grating spectrometer. We present detector count, spectral coverage and resolution, and give an update on the current status of the project. TIME was installed at the Arizona Radio Observatory 12 m telescope in 2019 and returned for further engineering, commissioning, and observing in 2022. Data taken during the 2022 season demonstrate the ability of TIME to compensate for field rotation through the use of a K-mirror system, as well as spectro-imaging functionality broadly in line with expectations given the current state of the instrument. TIME will return to ARO for science observations for the Winter 2024 season. We discuss hardware and software updates and preliminary data analysis in preparation for science scans.

Keywords: line intensity mapping, spectroscopy, mm-wavelength

1. INTRODUCTION

The Tomographic Ionized-carbon Mapping Experiment (TIME) aims to use the nascent technique of line intensity mapping (LIM; see recent reviews[1–3]) to map cosmic large-scale fluctuations in spectral line emissivities across time and space. Specifically, TIME targets [C II] emission from redshifts $z \approx 5$–9, measuring dust-obscured star formation as the universe emerges from the Epoch of Reionization (EoR). The 200–300 GHz observing window of TIME also encompasses emission from low- to mid-J CO rotational transitions at $z = 0.5$–2, meaning TIME will also be sensitive to cosmic molecular gas content during the epoch of peak cosmic star formation. TIME

Further author information: (Send correspondence to V.Butler)
E-mail: vlb59@cornell.edu

Millimeter, Submillimeter, and Far-Infrared Detectors and Instrumentation for Astronomy XII,
edited by Jonas Zmuidzinas, Jian-Rong Gao, Proc. of SPIE Vol. 13102,
131022G · © 2024 SPIE · 0277-786X · doi: 10.1117/12.3021442

is expected to carry out [C II] and CO LIM measurements at high statistical significance, with strong synergies with external galaxy survey datasets, further enhancing the insights gained into the two cosmic epochs being probed.[4]

As one of the first instruments specifically designed for CO/[C II] LIM, the TIME receiver represents a novel synthesis of CMB heritage and broadband spectroscopic technologies. The instrument, consisting of two spectrometers and nearly 2,000 TES Bolometers, developed in collaboration with JPL, has been characterized extensively at the Arizona Radio Observatory (ARO) on the 12m radio telescope at Kitt Peak, AZ. Here, we present on hardware and software updates that have primed us for LIM pathfinder surveys during our planned Winter 2024 deployment.

2. THE TIME INSTRUMENT

TIME is a millimeter-wave imaging spectrometer employing the WaFIRS architecture[5] previously demonstrated on Z-Spec,[6] with 2 banks of $R \sim 100$ curved grating spectrometers (one for each polarisation, with a polarising grid coupling both banks to the same lines of sight on sky), for a total of 32 independent single-beam single-polarization spectrometers, seen in Figure 1. Each spectrometer bank couples to 16 parallel plate waveguides which diffracts and focuses the broadband light from a feedhorn to the array of detectors. The linear array of feedhorns creates an instantaneous field of view 13.6 arcminutes long and one beam wide, with which TIME will undertake a $1.3^\circ \times 0.45'$ line scan for line intensity mapping.

The spectrometer banks have previously been described in Ref. 7. For this proceeding, we describe in further detail the detectors and receiver in subsection 2.1, and then the coupling optics for telescope operations in subsection 2.2.

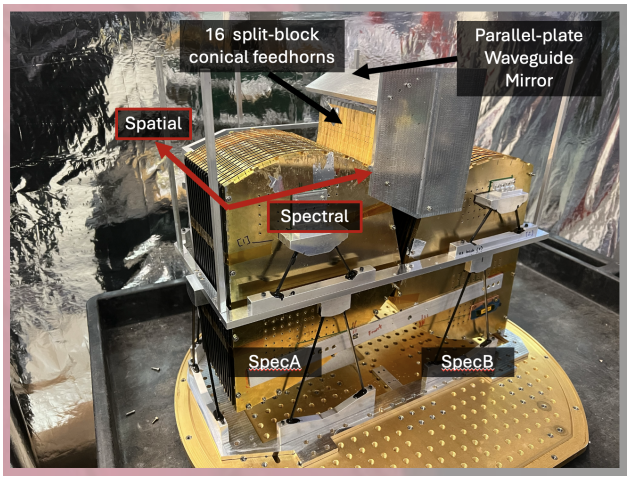

Figure 1. The TIME spectrometers mounted to a test plate, and held in place using a rigid stage assembly. During installation, the feedhorns point towards the ground.

2.1 The TIME Focal Plane and Receiver

The detection element of TIME is an array of 1920 silicon-nitride leg-isolated superconducting titanium transition-edge sensor (TES) bolometers, cooled to 250 mK and read out with NIST time-domain multiplexed SQUIDs and UBC multi-channel readout electronics (MCE). This architecture is reminiscent of the detection elements of CMB experiments, apart from the fact that the TIME focal plane is coupled to spectrometer banks.

The 200-300 GHz window is split equally between high frequency (HF) and low frequency (LF) gold-plated modules, which are each comprised of 4 detector subarrays. One such module is shown in Panel A of Figure 2. Each spectrometer bank contains 3 of each module type, for a total of 12 modules. The HF detectors are slightly smaller by design, allowing a larger pixel count per sub-array (48 HF and 32 LF). The properties of each module type are summarized in Table 1.

2.1.1 Lab Detector Characterization

Fabrication and assembly of the detector modules has become increasingly stable, producing larger fractions of functional detectors across the last two deployments. Our functional yield increased from 6% to 24% between 2019 and 2022. Recent lab testing using half of the full focal plane showed 57% of detectors had an ideal superconducting transition. This value would certainly have been higher except for some issues with the readout electronics along three of our readout rows. Due to their multiplexing setup, the detectors must be biased into the transition per column. Figure 3 shows load curves from just one column, where different detectors had diverse transition regions. Ideally, each curve would have overlapping peaks, but vary somewhat due to manufacturing

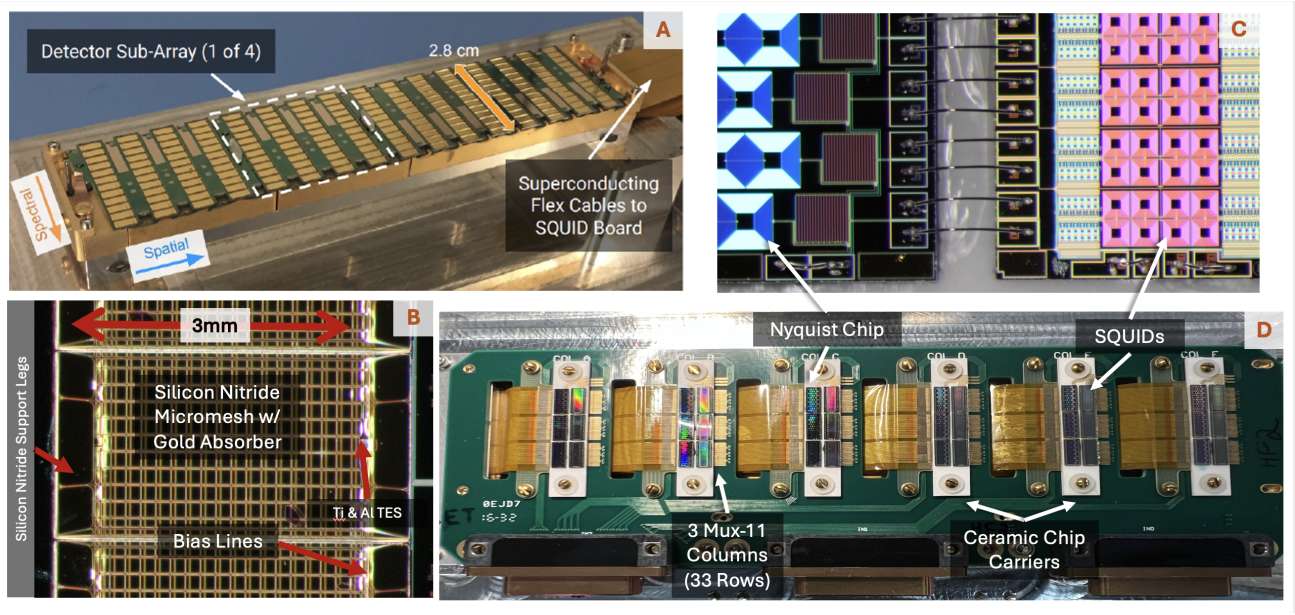

Figure 2. Layout of the detector and amplifier module components comprising the TIME focal plane. **(A)** The TIME detector module, designed by Jonathan Hunacek and created at the JPL microdevices laboratory by Clifford Frez and Anthony Turner. Each module contains 4 subarrays each with 4 multiplexed columns of individual detectors. The number of detectors varies across the high and low frequency subarrays. **(B)** Close-up of an individual TES Bolometer comprised of a gold absorber, Ti and AL TES, and silicon nitride support legs which suspend the absorber. **(D)** Amplifier SQUID module connected to the detector side through Kapton flex cables. The TIME architecture has 3 subarrays of Nyquist and SQUID chips (6 total), group in packets of 11 multiplexed rows for a total of 33. **(C)** Close-up of a single Nyquist and SQUID chip. The Nyquist chips were designed and fabricated at NIST.

Table 1. A partial summary of TIME instrument specifications.

Parameter	LF	HF
Spectral range (GHz)	183–230	230–325
End-to-end optical efficiency	0.2–0.25	0.2–0.25
Resolving power $\nu/\delta\nu$	90–120	90–120
Bolometer count / subarray	32 (1 pol. $\times$ 4 feeds $\times$ 8 chan.)	48 (1 pol. $\times$ 4 feeds $\times$ 12 chan.)
Bolometer count (total)	768 (2 pol. $\times$ 16 feeds $\times$ 24 chan.)	1152 (2 pol. $\times$ 16 feeds $\times$ 36 chan.)

and finite resistance of the flex cables. During our science observation, we will choose an optimal bias value to maximize the number of working detectors for a given column. We expect that revisions to the manufacturing process and the replacement of flex cables will improve this distribution.

Based on the geometry of our detectors, the ideal value of the thermal conductance G between the bolometers and their thermal bath would fall around 20 pW/K for low-frequency arrays and 30 pW/K for high-frequency arrays respectively at 450 mK. These design targets are optimized to achieve a photon noise level lower than the on-sky loading at our observation site as well as a desirable detector time constant for our science mission. As demonstrated in Figure 4, we determined G values by measuring the saturation power $P_{\rm sat}$ of each detector at multiple temperatures $T_{\rm bath}$. The relationship fit to the data in the left panel of the figure is represented by

$$P_{\rm sat} = \frac{G_c}{\beta+1}\frac{T_c^{\beta+1} - T_{\rm bath}^{\beta+1}}{T_c^{\beta}}, \tag{1}$$

where T_c is the critical temperature and $G_c \equiv G(T = T_c)$. We then derived G_{450} by the power-law dependence

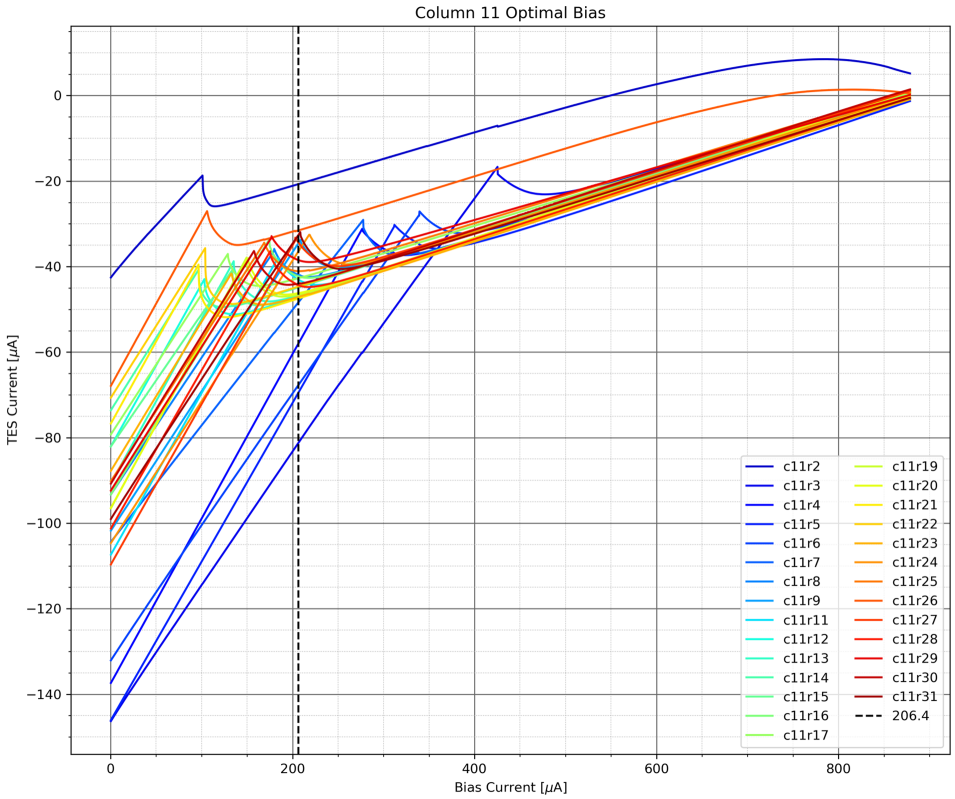

Figure 3. Optimal transition region identification for one column of detector load curves. Each color represents a different multiplexed row whose values range from 1–33. The vertical dashed line is an algorithmically determined transition bias that would maintain the maximum number of photon-sensitive bolometers. Each detector is swept from a high bias around 875 μA down to zero.

$G(T) \propto T^{\beta}$.

In general, our results show that low-frequency bolometers have a fairly uniform G distribution with a median hitting our design target. While the high-frequency bolometers also show a similar property, we were able to identify several subarrays with thermal shorts due to fabrication errors. We are using this information to motivate the fabrication process for the newest batches of detectors.

We were also able to characterize the optical efficiency η of the detectors. We calculated the optical efficiencies of the detectors using the change in power between two loading conditions by the equation

$$\eta = \frac{P_{\mathrm{sat,77K}} - P_{\mathrm{sat,300K}}}{(300\mathrm{K} - 77\mathrm{K})\, k_B \Delta\nu}\,, \tag{2}$$

where $\Delta\nu$ is the effective bandwidth of the detector channel, which we have previously characterized as ~ 1.5 GHz for nearly all detectors. Our two loading cases were Eccosorb layers immersed in liquid Nitrogen with an approximate temperature of 77 K, and room temperature at roughly 300 K. We ran this test on a recent batch of detector arrays which resulted in η values between 30–40% up to $\nu \sim 260$ GHz. With a new HF module design that yields a smaller backshort distance, we expect η to achieve the same values in the high frequency regime before gradually decreasing to zero at the end of the atmospheric window ~ 320 GHz due to the low-pass filter employed above the focal plane.

2.1.2 Superconducting Cryogenics

In order to achieve the superconducting operating temperature of 250 mK, the detectors are housed within a multi-staged closed-cycle cryostat. A Cryomech PT-415 4K refrigerator gets the focal plane to the temperature

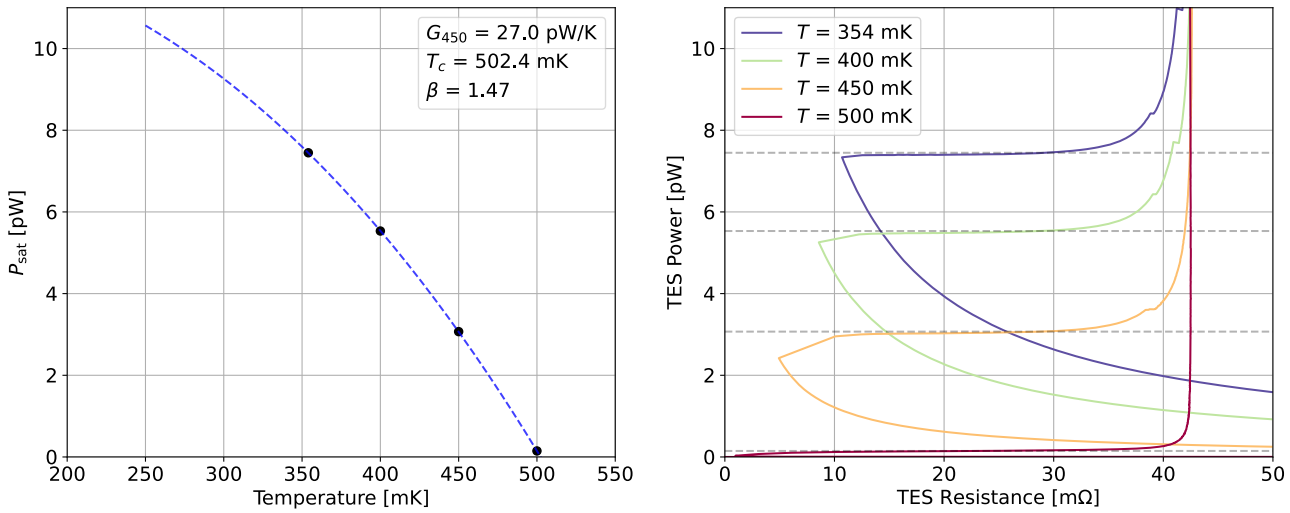

Figure 4. G measurements of a selected detector in a latest high-frequency array. *Right*: Saturation powers derived from detector load curves where the bias was swept from high to low values. Each color represents data from a single detector bias stepped at multiple bath temperatures. The horizontal dashed lines are the estimated saturation powers during detector transition regimes. *Left*: Saturation powers derived from the right plot versus temperature. The blue dashed line is the theoretical best fit to the data, from which we extract the fitting values of (G_{450}, T_c, β) displayed in the legend.

$<$ 4K. The 4K stage houses the cold pupil stop. A Joule Thompson Refrigerator is used to cool the third stage to 1K which also contains the polyethylene reimaging lens. The two lowest temperature stages, 350 mK and 250 mK, are cooled with a ^{3}He dual sorption system and a final ^{3}He system. To reduce the optical loading on the 350 mK stage dielectric blocking filters have been added at the 50 K and 4 K stages. A set of metal-mesh low-pass edge (LPE) filters are located at 350 mK and are used to define the upper end of the band.

2.2 Coupling Optics and K-Mirror

We have designed coupling optics to allow TIME to operate from the ARO 12 m Telescope, originally the ESO ALMA prototype antenna (which has led in the past to the ARO 12 m Telescope being referred to as the APA). Ref. 8 provides more detailed consideration of these optics, but we briefly summarise the key elements of the system, which we also show graphically in Figure 5.

The instrument is coupled to the telescope through a series of 6 mirrors. Three of those mirrors fold the optical path and relay the light to the focal plane via a cold reimaging lens that converts the $f/\#$ from 8 to 3. Minimization of spillover and optimization of image quality are key considerations in the design of these elements.

The remaining three mirrors are flat aluminum panels mounted to a rotating turret, shown as K1, K2, and K3 in Figure 5. Due to the altitude over azimuth mount of the ARO 12 m Telescope, the orientation of the focal plane rotates relative to the sky as sources move overhead. As the telescope tracks across the sky, the K-mirror assembly rotates counter to the direction of the sky rotation, keeping the detectors at constant orientation in right ascension and declination coordinates. Space constraints within the telescope cabin limit the rotation range of the K-mirror arm, which allows for approximately 9 continuous hours of observing time.

3. ENGINEERING AND COMMISSIONING OBSERVATIONS

We first fielded a partially integrated TIME receiver on the ARO 12 m Telescope in 2019. This engineering run revealed issues related to the cryogenic optics, which prevented the instrument from being able to properly focus. The cold lens design has since been revised. We also found that the TIME warm electronics picked up radio frequency interference that introduced significant readout noise, also since mitigated. Despite these issues, the 2019 run still allowed tests of communication between the TIME and ARO control systems, as well as tests of telescope tracking and scan patterns.

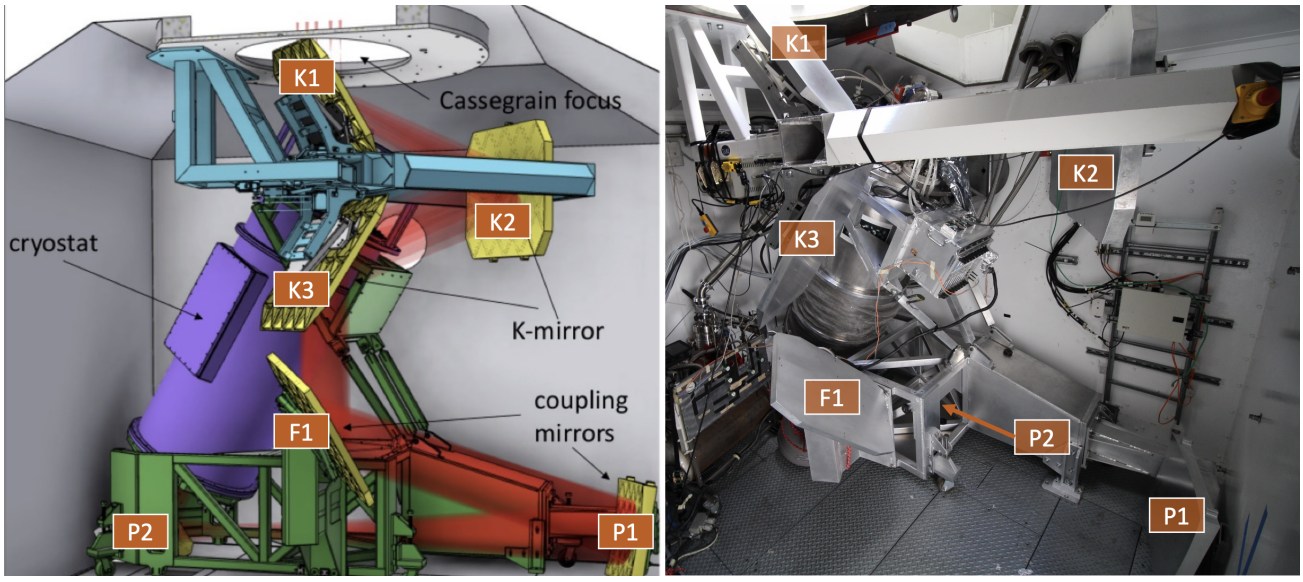

Figure 5. The red line in the left image shows the designed optical path connecting the cryostat to the Cassegrain focus of the telescope, which is through the ceiling of the cabin. The cryostat is shown in purple, mounted to an optical raft (green) which also holds the coupling mirrors. The three mirror assembly mounted to the ceiling is the image rotator. The right image shows the actual installation of these components in the ARO 12m cabin.

TIME was tested extensively at the ARO on-site lab prior to being installed again in the 12m telescope in January 2022, again in a partially integrated state. Commissioning tests were run through early February which helped confirm functionality of the instrument and identify residual issues both intrinsic and extrinsic to the receiver. These tests are discussed in the following sections. It was also at this deployment that TIME started observing more sources with significant spectral line emission in our bands. At local redshifts, TIME is sensitive to a range of molecular gas tracers, including the ^{12}CO(2–1) rotational transition, the ^{13}CO(2–1) isotopologue, the H^{12}CN(3–2) transition tracing denser molecular gas, and its own H^{13}CN(3–2) isotopologue. Observations demonstrate the sensitivity of our instrument to these emission lines from observations of various Galactic regions. These observations were also the first application of our remote observing capabilities, motivated by the COVID-19 pandemic.

3.1 On-Sky Optical Characterization

Observations of bright sources at a range of altitude and azimuth positions confirmed that K-mirror tracking compensates for sky rotation and keeps the linear detector array aligned with all feedhorns at constant declination. Figure 6 is produced by co-adding maps of Jupiter, showing the alignment of 14 of our feeds. We plan to use observations of Jupiter in future for other purposes, such as characterisation of sidelobes from reflections in the system and absolute calibration.

During the comissioning test we estimated the beamwisth using observations of Mars. Measurements of Mars provide a better estimate the main beamwidth of TIME compared with observations of Jupiter because there is a reduced need to accurately model its smaller intrinsic angular size (a little over four arcseconds). The measurements of the beamwidth from Mars are shown in the left panel of Figure 7.

The right panel of Figure 7 shows estimates of the beam FWHM per detector. We largely see expected trends, with detectors at the edges of the focal plane having wider beams, and detectors near boresight broadly matching the approximate expected beam width of $1.2\lambda/D$ (with $D = 12$ m). Residuals may be attributed to incomplete focus optimisation resulting in slight broadening of the beams.

3.2 Spectro-Imaging Performance

Figure 8 shows broadband images of Galactic star-forming regions, showing that coadding across our online detectors, we are able to make maps of these regions that resolve diffuse features beyond the principal bright

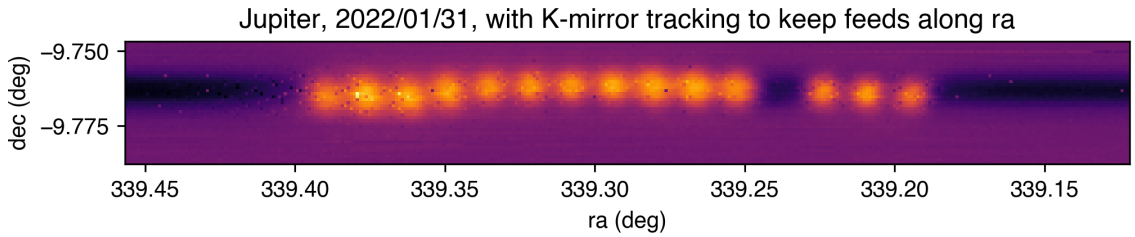

Figure 6. Visualisation of 14 (non-dark and responsive) TIME feeds on the sky in boresight right ascension (RA) and declination coordinates, using an observation of Jupiter. The K-mirror tracking keeps the feeds aligned along a line of constant declination in this (constant-DEC, RA-scanning) raster, with some deviations due to distortions introduced by aberrations in the receiver optics.

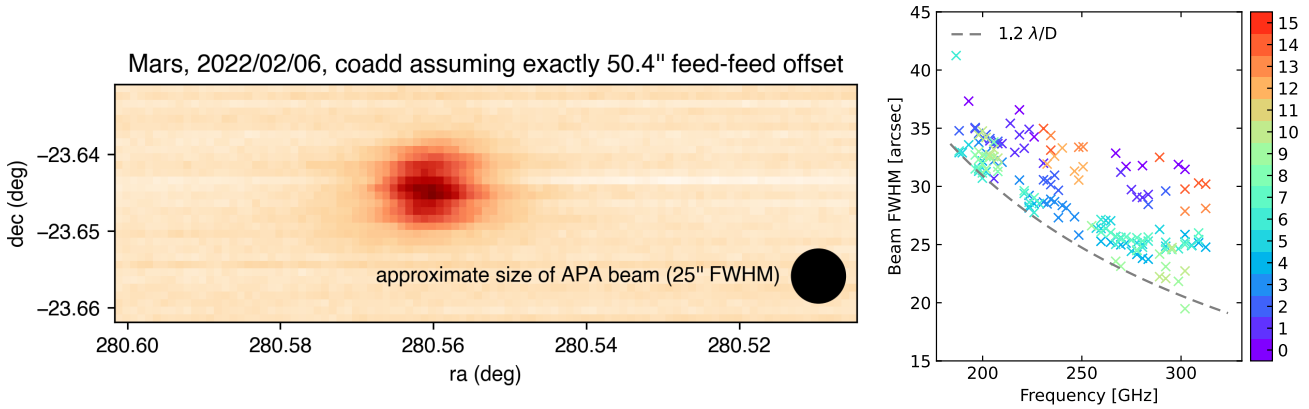

Figure 7. Reductions of observations of Mars. *Left:* Coadded image of Mars assuming that the feeds see the same declination and are offset in RA by exactly 50.4", which is more or less the expectation *a priori*. We essentially recover a bright source with the apparent angular size corresponding approximately to the expected size of the beam based on the size of the telescope. *Right:* Full widths at half maximum of the on-sky beam of each detector, inferred from maps of Mars. Colours indicate the corresponding feed, with feeds 7 and 8 nearest to boresight. Values obtained for feeds near boresight are within 10–20 percent of the expectation of $1.2\lambda/D$ (given wavelength λ and $D = 12$ m for the ARO 12 m Telescope, and assuming underillumination of the primary with ≈ 15 dB edge taper).

clumps. We also provide a clear demonstration of spectro-imaging in Figure 9 with an observation of the Sagittarius A region. The Central Molecular Zone of the Galaxy features bright, broad ($\gtrsim 100$ km s^{-1}) CO emission lines[9,10] clearly seen by TIME. After masking channels sensitive to CO(2–1), we can still clearly recover the underlying clumps and circumnuclear disk with their differing spectral indices.

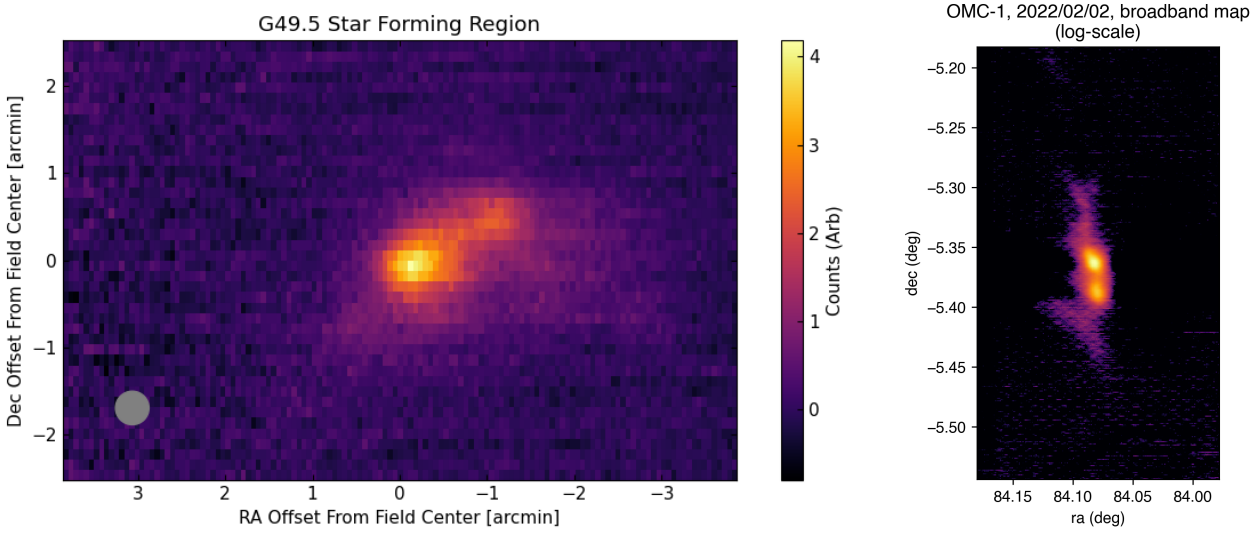

Figure 8. A sample of continuum images obtained with TIME during the 2022 commissioning tests, coadding across all detectors online and responsive at the time of each observation. *Left:* Image of the G49.5 star forming region, showing diffuse features beyond the main clump. The grey circle indicates the approximate size of the TIME beam. *Right:* Image of the OMC-1 region in the Orion molecular cloud complex. We show the intensity in a log colour scale to highlight the low noise and the ability to once again resolve diffuse low-brightness features beyond the main clumps of the region.

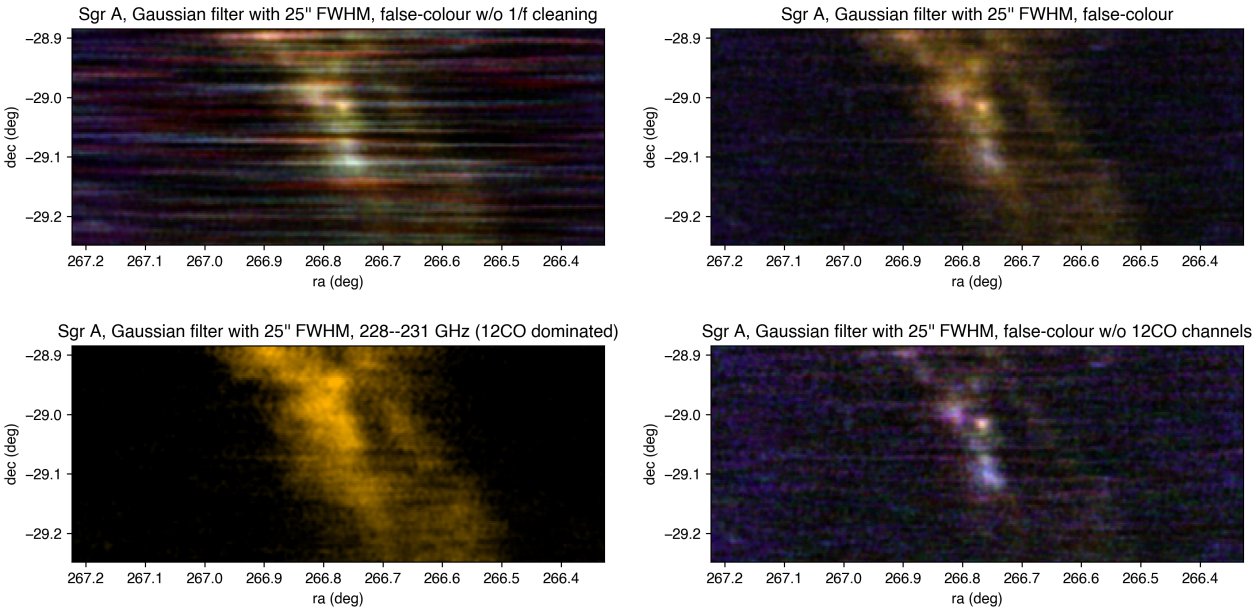

Figure 9. Galactic Center, Sgr A, false color images. The upper left image shows the observation prior to removal of correlated noise. Subtraction of common-mode templates from each detector timestream results in the image on the upper right, with the correlated noise mitigated significantly. An orange-yellow glow dominates this image, originating from bright and broad CO(2–1) emission at 230 GHz clearly sensed by TIME spectro-imaging. Separating out the frequency channels corresponding to CO emission (lower left) leaves behind a more continuum-dominated image (lower right), where the difference in hue between the circumnuclear disk and surrounding molecular clumps reflects the different spectral indices of continuum emission from these components of the Sgr A complex.

3.3 Suppression of Correlated Noise

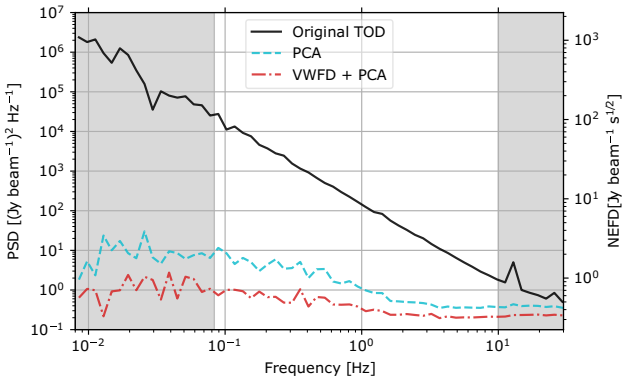

Figure 10. Power spectral densities of timestreams obtained from a test observation at Kitt Peak. The original time-ordered data (TOD) shows $1/f$ noise dominating over uncorrelated noise, whereas a PCA filter suppresses the contribution of this $1/f$ noise by many orders of magnitude. The unshaded region indicates the range of frequencies corresponding to angular scales of primary interest for TIME scanning observations.

The TIME commissioning tests reveal time-domain and inter-detector correlations in observation timestreams due to a combination of coherent fluctuations in the atmosphere and the TIME instrument elements (including in the readout chain), often modulated by the telescope scanning. Many of these are entirely anticipated either a priori or based on lab testing, and can be mitigated upstream of data analysis through appropriate choices in observing strategy and instrument integration. However, we also continue to develop new strategies to further mitigate correlated noise within our map-making pipeline.

Figure 10 demonstrates a realistic limit in suppressing correlated noise through analysis. The raw time-ordered data (TOD) has significant time-domain correlations from a combination of atmospheric fluctuations and instrumental gain drifts, shown by the power-law (or '$1/f$') noise power spectral density (PSD). However, a principal component analysis[11] (PCA) can identify inter-detector common-mode fluctuations for filtering, significantly mitigating this $1/f$ noise. We can further reduce correlated noise by pre-processing the timestreams with a large-timescale variable-window fixed-degree (VWFD) polynomial detrender.[12] We thus demonstrate suppression of $1/f$ noise by several orders of magnitude in PSD, which is necessary for the highly sensitive line-intensity mapping observations that comprise the primary science case for TIME. The mapmaking pipeline applied to commissioning observations shown in subsection 3.2 does not employ filtering nearly as extreme as what is used for Figure 10, given the targets were bright Galactic sources, with the Sgr A mapmaking demonstrated in Figure 9 employing a much less severe, non-PCA approach to common-mode filtering.

Further investigations in simulation and with future data will help us better understand the optimal balance between severe removal of correlated timestream noise with signal loss.

4. CONCLUSION

TIME, a waveguide grating spectrometer with CMB-style TES-bolometry, has been deployed multiple times at the ARO 12m telescope. Most recently, it was used to study the Galactic center, while also characterizing our ability to perform remote observing, utilize the K-mirror field de-rotator, and test our spectral sensitivities using a new map-making pipeline. In preparation for the Winter 2024 deployment, we have been designing a more robust stage to hold the spectrometers stable while the telescope cabin tilts, iterating and testing new bolometer designs from JPL, and improving our cryogenic cycling procedure. Based on lab testing, we should have a hold time of roughly 72 hours between fridge cycles, enabling high observing efficiency in line-intensity mapping observations to achieve our scientific goals.

We have also been in close contact with the ARO following the 2022 Contreras Fire, which burned down all personnel lodging and facilities, while leaving the telescope, dome, and adjacent lab untouched. Everything is in good order for a resumption of normal research activities. TIME thus continues to progress towards illuminating the cosmic epochs of reionization and peak star formation.

ACKNOWLEDGMENTS

The hardware in this work is supported by National Science Foundation award number 1910598 under the NSF-ATI program and the software and data analysis by 2308039 under the NSF-AAG program. Part of the research described in this proceeding was carried out at the Jet Propulsion Laboratory, California Institute of Technology, under a contract with the National Aeronautics and Space Administration. NE, RPK, IL, ECM, and DPM were supported by the National Science Foundation through CAREER grant AST-1653228. RPK was supported by the National Science Foundation through Graduate Research Fellowship grant DGE-1746060. DTC was supported by a CITA/Dunlap Institute postdoctoral fellowship. The Dunlap Institute is funded through an endowment established by the David Dunlap family and the University of Toronto. TCC and GS acknowledge support from the JPL Strategic R&TD awards. AC acknowledges support from NSF AST-1313319 and 2015-2016 UCI Office of Research Seed Funding Award.

The UArizona ARO 12-meter Telescope on Kitt Peak is operated by the Arizona Radio Observatory (ARO), Steward Observatory, University of Arizona.

REFERENCES

[1] Kovetz, E. D., Viero, M. P., Lidz, A., Newburgh, L., Rahman, M., Switzer, E., Kamionkowski, M., Aguirre, J., Alvarez, M., Bock, J., Bond, J. R., Bower, G., Bradford, C. M., Breysse, P. C., Bull, P., Chang, T.-C., Cheng, Y.-T., Chung, D., Cleary, K., Corray, A., Crites, A., Croft, R., Doré, O., Eastwood, M., Ferrara, A., Fonseca, J., Jacobs, D., Keating, G. K., Lagache, G., Lakhlani, G., Liu, A., Moodley, K., Murray, N., Pénin, A., Popping, G., Pullen, A., Reichers, D., Saito, S., Saliwanchik, B., Santos, M., Somerville, R., Stacey, G., Stein, G., Villaescusa-Navarro, F., Visbal, E., Weltman, A., Wolz, L., and Zemcov, M., "Line-Intensity Mapping: 2017 Status Report," *arXiv e-prints* , arXiv:1709.09066 (Sept. 2017).

[2] Kovetz, E., Breysse, P. C., Lidz, A., Bock, J., Bradford, C. M., Chang, T.-C., Foreman, S., Padmanabhan, H., Pullen, A., Riechers, D., Silva, M. B., and Switzer, E., "Astrophysics and Cosmology with Line-Intensity Mapping," *Bulletin of the AAS* **51**, 101 (May 2019).

[3] Bernal, J. L. and Kovetz, E. D., "Line-Intensity Mapping: Theory Review," *arXiv e-prints* , arXiv:2206.15377 (June 2022).

[4] Sun, G., Chang, T. C., Uzgil, B. D., Bock, J. J., Bradford, C. M., Butler, V., Caze-Cortes, T., Cheng, Y. T., Cooray, A., Crites, A. T., Hailey-Dunsheath, S., Emerson, N., Frez, C., Hoscheit, B. L., Hunacek, J., Keenan, R. P., Li, C. T., Madonia, P., Marrone, D. P., Moncelsi, L., Shiu, C., Trumper, I., Turner, A., Weber, A., Wei, T. S., and Zemcov, M., "Probing Cosmic Reionization and Molecular Gas Growth with TIME," *Astrophys. J.* **915**, 33 (July 2021).

[5] Bradford, C. M., Naylor, B. J., Zmuidzinas, J., Bock, J. J., Gromke, J., Nguyen, H., Dragovan, M., Yun, M., Earle, L., Glenn, J., Matsuhara, H., Ade, P. A. R., and Duband, L., "WaFIRS: a waveguide far-IR spectrometer: enabling spectroscopy of high-z galaxies in the far-IR and submillimeter," in [*IR Space Telescopes and Instruments*], Mather, J. C., ed., *Society of Photo-Optical Instrumentation Engineers (SPIE) Conference Series* **4850**, 1137–1148 (Mar. 2003).

[6] Bradford, C. M., Ade, P. A. R., Aguirre, J. E., Bock, J. J., Dragovan, M., Duband, L., Earle, L., Glenn, J., Matsuhara, H., Naylor, B. J., Nguyen, H. T., Yun, M., and Zmuidzinas, J., "Z-Spec: a broadband millimeter-wave grating spectrometer: design, construction, and first cryogenic measurements," in [*Z-Spec: a broadband millimeter-wave grating spectrometer: design, construction, and first cryogenic measurements*], Bradford, C. M., Ade, P. A. R., Aguirre, J. E., Bock, J. J., Dragovan, M., Duband, L., Earle, L., Glenn, J., Matsuhara, H., Naylor, B. J., Nguyen, H. T., Yun, M., and Zmuidzinas, J., eds., *Society of Photo-Optical Instrumentation Engineers (SPIE) Conference Series* **5498**, 257 (Oct. 2004).

[7] Li, C.-T., Bradford, C. M., Crites, A., Hunacek, J., Wei, T., Cheng, J.-C., Chang, T.-C., and Bock, J., "TIME millimeter wave grating spectrometer," in [*Millimeter, Submillimeter, and Far-Infrared Detectors and Instrumentation for Astronomy IX*], Zmuidzinas, J. and Gao, J.-R., eds., **10708**, 107083F, International Society for Optics and Photonics, SPIE (2018).

[8] Trumper, I., Aftab, M., and Kim, D. W., "Freeform surface selection based on parametric fitness function using modal wavefront fitting," *Optics Express* **27**, 6815 (Mar. 2019).

[9] Bally, J., Stark, A. A., Wilson, R. W., and Henkel, C., "Galactic Center Molecular Clouds. I. Spatial and Spatial Velocity Maps," **65**, 13 (Sept. 1987).

[10] Bally, J., Stark, A. A., Wilson, R. W., and Henkel, C., "Galactic Center Molecular Clouds. II. Distribution and Kinematics," *Astrophys. J.* **324**, 223 (Jan. 1988).

[11] Greenacre, M., Groenen, P. J. F., Hastie, T., D'Enza, A. I., Markos, A., and Tuzhilina, E., "Principal component analysis," *Nature Reviews Methods Primers* **2**, 100 (Dec. 2022).

[12] LJUNG, G. M. and BOX, G. E. P., "On a measure of lack of fit in time series models," *Biometrika* **65**, 297–303 (08 1978).